

# LiquiRIS: A Major Step Towards Fast Beam Switching in Liquid Crystal-based RISs

Luis F. Abanto-Leon<sup>\*§</sup>, Robin Neuder<sup>†§</sup>, Waqar Ahmed<sup>¶</sup>, Alejandro Jimenez Saez<sup>†</sup>, Vahid Jamali<sup>†</sup>, Arash Asadi<sup>‡</sup>  
<sup>\*</sup>Ruhr University Bochum, <sup>†</sup>TU Darmstadt, <sup>¶</sup>Fachhochschule Dortmund, <sup>‡</sup>TU Delft

**Abstract**—Reconfigurable intelligent surfaces (RISs) offer enhanced control over propagation through phase and amplitude manipulation but face practical challenges like cost and power usage, especially at high frequencies. This is specifically a major problem at high frequencies (Ka- and V-band) where the high cost of semiconductor components (i.e., diodes, varactors, MEMSs) can make RISs prohibitively costly. In recent years, it is shown that liquid crystals (LCs) are low-cost and low-energy alternative which can address the aforementioned challenges but at the cost of lower response time. In LIQUIRIS, we enable leveraging LC-based RIS in mobile networks. Specifically, we devise techniques that minimize the beam switching time of LC-based RIS by tapping into the physical properties of LCs and the underlying mathematical principles of beamforming. We achieve this by modeling and optimizing the beamforming vector to account for the rotation characteristics of LC molecules to reduce their transition time from one state to another. In addition to prototyping the proposed system, we show via extensive experimental analysis that LIQUIRIS substantially reduces the response time (up to 70.80%) of liquid crystal surface (LCS).

## I. INTRODUCTION

Reconfigurable intelligent surfaces (RISs) act as tuneable reflectors or scatterers that can manipulate the propagation of radio waves by adjusting the phase, amplitude, and direction of the reflected waves. RISs are projected to enhance the overall performance of wireless system including signal strength, range, and capacity. The prospect of deploying RISs in diverse environments, such as homes, public spaces, and even smart cities, holds the promise of transforming how we communicate and interact with the wireless world. *Although the theoretical foundations of RISs are promising, much work remains to be done to bring this concept to reality.*

**Existing prototypes and their limitations.** In the past few years, we have observed several attempts in prototyping and experimental evaluation of RISs mostly at sub-6GHz frequencies [1], [2], [3], [4], [5], [6], [7], [8] and a few exceptions at higher frequencies, e.g., 28GHz [9], 60GHz [10]. These prototypes are almost exclusively semiconductor-based, i.e., they rely on PIN diodes [8], [9], [11], [12], varactors [13], [14], [15], or micro-electro-mechanical systems (MEMS) [16] for phase shifting. Several limiting factors in the above-mentioned work can significantly hinder the large-scale deployment of RISs, which are outlined in the following.

- *High power consumption.* Both PIN diodes and varactors have high power consumption, making large RISs power-hungry devices.

- *High fabrication cost.* The manufacturing cost of an RIS quadratically increases with the surface area. This increase is attributed to the required number of diodes, i.e., one diode per bit per radiating element. Despite continuous advances in packaging, integrating thousands of discrete RF components in large surfaces in a reliable and cost-effective manner is still an open challenge [8]. The high-cost issue is also present for MEMS, although they have lower power consumption.
- *Limited phase resolution.*<sup>1</sup> The granularity of the RIS's control over the reflected signal phase is usually related to the number of bits available for phase quantization. For instance, in PIN diode-based designs, the achievable number of bits is dictated by the number of PIN diodes used for each RIS unit cell.

In recent years, it has been demonstrated that liquid crystals (LCs) offer a low-cost and low-energy alternative to tackle the mentioned limitations. In fact, LC-based RISs will be significantly more cost-effective than the semiconductor-based alternatives since they do not rely on high-frequency electronic components. In fact, it is expected that the manufacturing cost of liquid crystal surfaces (LCSs) will reduce to that of a commercial liquid crystal display (LCD) television for which the manufacturing process of LCDs is highly developed. However, using LCs in mobile networks comes with its own challenges.

**Challenges.** In principle, phase shifting in LCs occurs through the electrically-induced mechanical rotation of LC molecules. It is this mechanical rotation that causes a certain response time<sup>2</sup> of the LC microwave components. Addressing the response time remains an open challenge in particular in the context of mobile networks. The state of the art currently aims at lowering the response time by designing more suitable LC material/molecules and/or making structural changes by engineering thinner LC layers for phase shifters. Although effective, both approaches have their limitation. Designing new LC mixtures can be a very long research endeavour and reducing thickness of the LC layer makes it prone to manufacturing tolerances, which can be a major issue in large surfaces. Another approach consist in the so-called overshooting [17], a technique that applies high voltages to the LCS unit cells,

<sup>1</sup>While it has been shown in the literature that 1- or 2-bit RIS phase-shift resolution may be sufficient to achieve simple objectives, e.g., maximizing the main-lobe gain, higher phase-shift resolutions may be needed in sophisticated settings such as (side-lobe) interference control in multi-user scenarios.

<sup>2</sup>The response time refers to the time it takes for the LC molecules to reorient themselves in response to biasing voltage.

<sup>§</sup>Both authors contributed equally to this research

accelerating the rotation of the LC molecules and thereby promoting swifter phase changes. However, overshooting alone is insufficient as it reduces the response time per element only to a certain degree and neglects the fact that the RIS response time to switch to a desired reflection pattern can be further minimized by the joint configuration of all its elements.

**LIQUIRIS.** We propose a novel approach that complements prior works, which focus on hardware-design enhancement, by looking into the challenge of response time reduction from an algorithmic and communication point of view. Specifically, we propose a solution to reduce the response time of LC-based RISs by *tapping into the physical properties of LCs and the underlying mathematical principles of beamforming*. As mentioned, the slow response times of LCSs stem from the slow rotation of LC molecules. By characterizing and modeling this physical phenomenon, we formulate and optimize the beamforming<sup>3</sup> such that it account for the rotation of LC molecules and their characteristics. To our knowledge, LIQUIRIS is the first work proposing this approach for LC response time optimization. We elaborate on this in the following.

Fig. 1a and Fig. 1b depict the time an LCS unit cell needs to change its phase from  $0^\circ$  to  $360^\circ$  (positive phase shift) and from  $360^\circ$  to  $0^\circ$  (negative phase shift), respectively. Particularly, a positive phase shift is achieved faster than a negative phase shift. For instance, it takes approximately 20 ms to transition from  $0^\circ$  to  $320^\circ$  whereas it takes about four times more, i.e., approximately 80 ms, to shift from  $-320^\circ$  to  $0^\circ$ . This occurs because *a positive phase shift is achieved by applying an electrical force on the LC molecules, whereas a negative phase shift is achieved by the mechanical realignment of LC molecules in the absence of the applied electric field, which is significantly slower*.

Inspired by these properties, we design LC-specific beamforming, whose phase-shift reconfiguration is optimized for the transition characteristics of LCSs. From an optimization point of view, the design of LCS phase shifts is essentially a multi-variable optimization problem, which may have different phase-shift solutions for a given objective. For instance, the shape of the reflected beam does not change by adding a constant phase offset to all unit cells. *Current RIS phase-shift design algorithms are designed for semiconductors and do not account for the physical characteristics of LCs*. Thus, if these algorithms are directly applied to the LCS phase-shift design, they may lead to a solution for which the LCS requires a significant time for transitioning from the current phase-shift configuration to the newly designed one, *thus significantly increasing the beam switching time*. To enable a fast transition, the new LCS phase shifts should be designed such that the design objective (e.g., anomalous reflection along a desired direction) is achieved with *minimum* changes to the current phases. More specifically, from the possible solutions of the phase-shift optimization problem, we find the one that realizes a faster response time. *LIQUIRIS is the first work tackling*

<sup>3</sup>In this article, we refer to the time needed to move from one *beamforming* configuration/vector to another as *response time*. While this essentially translates to *beam switching* delay, we chose to use the more technically suitable term of response time in this article.

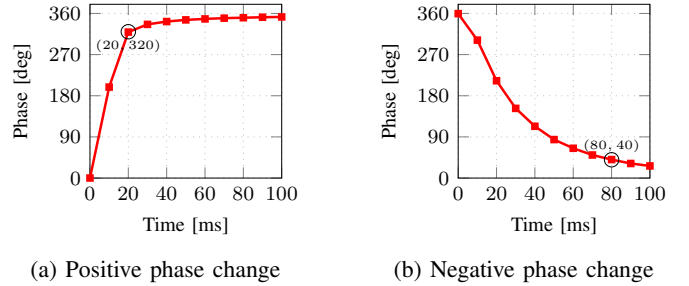


Figure 1: Response time of an LCS unit-cell. Positive phase changes are achieved faster than negative ones.

*this problem*. Motivated by this discussion, we present two LCS-specific solutions, namely LIQUIRIS-SINGLEBEAM and LIQUIRIS-JOINTBEAM.

**Contributions.** In summary, our main contributions are:

- LIQUIRIS is the first work analyzing the potential of LC technology for RIS design. To this aim, we conduct a thorough study of the physics of LCs and develop an analytical model to relate the response time of the LCSs to the beamforming design.
- Based on our model, we devise two solutions, namely, LIQUIRIS-SINGLEBEAM and LIQUIRIS-JOINTBEAM, which optimize the response time when designing the beamforming vectors.
- We prototype an LCS and show via extensive experimental evaluation that our proposed method can significantly reduce the response time (up to 70.80%).

## II. PHYSICAL PRINCIPLES OF LC TECHNOLOGY

**Phase shifting capability.** Based on its electromagnetic anisotropy, LC features varying permittivities for different orientations of its molecules towards the radio-frequency (RF) electric field. This characteristic is caused by the molecule's ellipsoidal shape, resulting in the following behavior: LC exhibits a larger permittivity (i.e., higher phase shift) when the electric field,  $\vec{E}_{\text{RF}}$ , is aligned with the major axis of the molecules,  $\vec{n}$ , which makes the device electrically larger due to the higher permittivity. If  $\vec{E}_{\text{RF}}$  is oriented perpendicular to  $\vec{n}$ , LC exhibits a lower permittivity (i.e., lower phase shift) and the device becomes electrically smaller.

The phase shift of RF signals can be altered by applying a DC or low kHz bias voltage to control the orientation of the LC molecules. For this, a thin LC-layer is placed between two electrodes. When not biased, the LC molecules align perpendicular to the RF-electric field (i.e.,  $\vec{n}$  is aligned perpendicular to  $\vec{E}_{\text{RF}}$ , see Fig. 2 on the top right). The LC permittivity corresponds to  $\varepsilon_{r,\perp}$ . When the biasing voltage increases, the LC molecules start to align with the applied bias voltage until the saturation voltage is reached. Then, the LC molecules are oriented in parallel to the RF-electric field (i.e.,  $\vec{n}$  is aligned parallel to  $\vec{E}_{\text{RF}}$ , see Fig. 2 on the bottom right) and the permittivity of the LC corresponds to  $\varepsilon_{r,\parallel}$ . The permittivity can be continuously tuned between  $\varepsilon_{r,\perp}$  and  $\varepsilon_{r,\parallel}$  by altering the bias voltage between 0 and the saturation

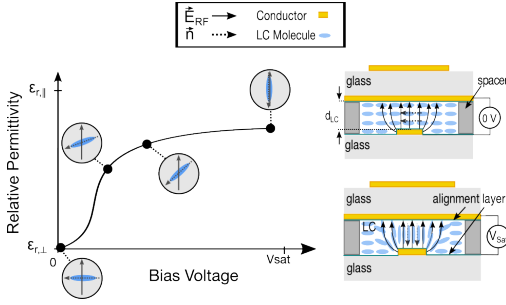


Figure 2: LC relative permittivity versus biasing voltage (left). Microstrip assembly depicting LC biasing in unbiased and fully biased states (right).

voltage,  $V_{sat}$ . The maximum achievable phase shift scales with  $\Delta\epsilon = \epsilon_{r,\parallel} - \epsilon_{r,\perp}$ .

**Response time.** While the rotation of LC molecules from  $\epsilon_{r,\perp}$  towards  $\epsilon_{r,\parallel}$  is achieved by increasing the bias voltage, a different mechanism is required for the rotation from  $\epsilon_{r,\parallel}$  towards  $\epsilon_{r,\perp}$ . For this purpose, a thin alignment layer is applied. A thin alignment layer with grooves creates mechanical anchoring forces, facilitating LC molecule realignment. However, applying bias voltage aligns LC along electrodes faster than molecule alignment due to these forces. The latter slow transition is considered and modelled by the decay or switch-off response time,  $\tau_{off}$ , which depends on the LC mixture and the LC layer thickness,  $d_{LC}$ . The response time increases quadratically with  $d_{LC}$ . Hence, the response time can be reduced drastically by adopting narrower LC layers. Due to fabrication tolerances,  $d_{LC}$  typically does not get thinner than few  $\mu\text{m}$ , which corresponds to switch-off response times in the order of tens of milliseconds for common LC mixtures such as GT7-29001 from Merck KGaA<sup>4</sup>.

### III. LIQUIRIS DESIGN

In this section, we first present the architecture of our LCS. Subsequently, we introduce the LCS fabrication process, as well as the characterization result of our LCS. The findings build upon the prototype outlined in Ref. [18].

#### A. LCS architecture

Two architectures exist for LCS: resonant and delay line [19]. In the resonant architecture, the LC layer is positioned between a resonating element and a ground plane, combining phase shifting and radiating properties in one layer. Despite its simple design and fabrication advantages, this architecture struggles to achieve wide bandwidth ( $> 5\%$ ), fast response time (ms), and low losses ( $< 6$  dB) simultaneously. Therefore, we opt for the delay line architecture which requires a dedicated phase shifter for each element (Fig. 3a). Though this necessitates an additional design step, it separates phase shifting and radiating properties, allowing for optimization tailored to specific requirements, including wide bandwidth, fast response time, and low losses.

<sup>4</sup><https://www.merckgroup.com/en/news/liquid-crystal-smart-antennas-29-03-2021.html>

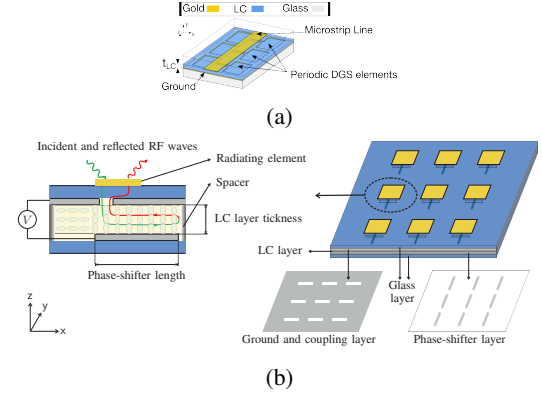


Figure 3: Illustration of: (a) DGS-IMSL based nematic LC phase shifter and (b) the architecture of LIQUIRIS.

The thin LC layer is usually filled between two layers of glass. Glass is most commonly used as a substrate since it provides a smooth, flat surface that is required for a stable, well-defined LC thickness over large panels. In addition, the glass substrates enable the direct growth of metal circuitry on their surfaces. Each glass substrate experiences a selective metallization process on one or both sides, enabling the precise patterning of desired circuit components such as bias control lines, radiating elements and biasing electrodes. In the context of guiding RF-waves, metals with high conductivity such as copper or gold are preferred. Conversely, for the implementation of bias control lines, Indium-Tin-Oxide (ITO) is commonly utilized due to its high resistivity.

Typically, one of the glass substrates is metallized to function as a ground layer. Concurrently, the other glass substrate undergoes selective metallization to facilitate the introduction of phase-shifting control voltage into individual unit cells, as illustrated in Fig. 3b. This configuration enables the independent manipulation of phase shifts across the device, offering enhanced control and versatility. To establish effective coupling between the phase shifter and free space, a radiating element must be integrated. Common radiating elements are patch or dipole antennas, serving as interfaces between the phase shifter and the surrounding environment, thus enabling signal transmission and reception.

To implement dedicated phase shifters, it is essential to employ transmission line topologies that align with LCD manufacturing standards. One of these transmission lines is the inverted microstrip line in which the transmission line is terminated with a reflective end in order to reflect the wave towards the radiating antenna. As a result, the wave propagates twice through the phase shifter. A suitable solution to implement the termination is the abrupt termination of the metal strip in an open end. As the phase shifter must fulfill strict requirements to be suitable for the LCS, such as high compactness, low losses and fast response time, the performance of a conventional inverted microstrip line does not suffice for its implementation in an LCS based on the delay line architecture. As a result, we employ a more sophisticated phase-shifting topology, the defective ground structure inverted

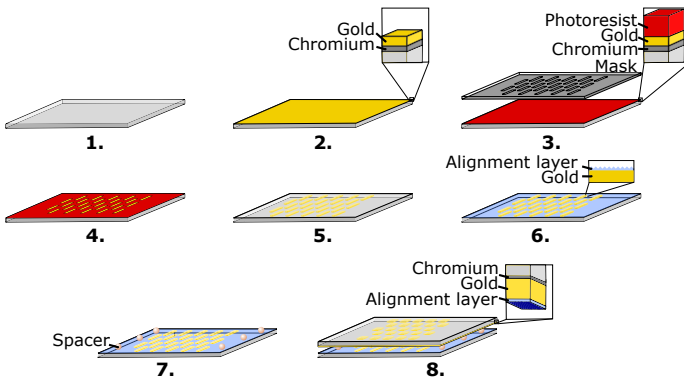


Figure 4: Overview of key stages of the LCS fabrication.

microstrip line (DGS-IMSL), which improves the phase-shifting performance by introducing defects in the metallic ground plane.

### B. LIQUIRIS fabrication

LIQUIRIS is prototyped on glass using a multistep process involving several key stages, as illustrated in Fig. 4 and we briefly describe here:

- 1) **Glass sample preparation.** We first prepare the sample for the subsequent fabrication steps by careful cleaning.
- 2) **Thin film evaporation.** In order to structure the glass samples, we evaporate thin films with thicknesses of tens of nm of metal (i.e. chromium and gold) which constitute a seed layer for the following steps.
- 3) **Photolithography.** A photolithographic step is employed to define the desired pattern for the RIS. We apply a photoresist on the seed layer, and a photomask with the desired pattern is placed on top. The device is then exposed to ultraviolet (UV) light, which selectively cures the photoresist in the exposed areas.
- 4) **Electroplating.** The metal layers are selectively grown by electroplating on the pattern previously defined by the photomask.
- 5) **Removal of seed layer.** The thin seed layers can now be removed with suitable etchants.
- 6) **Alignment Layer coating.** The structures are coated with a thin film of the alignment layer (approximately 100 nm) which is subsequently patterned to form grooves. This can be achieved by mechanical rubbing, for example.
- 7) **Spacers.** To provide a certain layer thickness  $d_{LC}$  spacers are required between the two glass plates. Commonly, these spacers are micropearls with a defined diameter.
- 8) **Bonding.** The second glass layer is prepared with steps 1 to 7. Next, both glass plates (i.e., microstrip and ground layer) are aligned and bonded together with a suitable adhesive.

Finally, the edges of the substrates are sealed to prevent leakage and maintain the integrity of the device. LC is filled into the gap of the glass substrates in a vacuum chamber.

### C. Characterizing LIQUIRIS

As a next step, we characterize the unit cell bandwidth and overall beampatterns of LIQUIRIS ranging from  $-60^\circ$  to  $60^\circ$ .

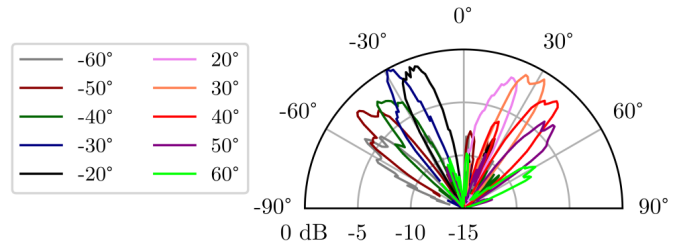


Figure 5: Measured beamsteering capabilities of LCS at 61GHz. The magnitude is normalized to the maximum received signal of  $\approx -45$  dB. The noise floor is  $\approx -59$  dB.

**III-C1 Phase shifter characterization:** The phase shifter design and characterization is crucial for the delay line architecture. Hence, phase shifter designs have to be evaluated first in an electromagnetic simulation software, such as CST Studio Suite or HFSS, and, afterwards, the results have to be verified in measurements. The employed DGS-IMSL phase shifter topology provides several advantages: It combines the thin LC-layer and hence, comparably fast response times, with low losses and a high compactness. In addition, the topology can be easily scaled towards desired frequency ranges. The insertion loss of the phase shifter for thin  $d_{LC}$ , specifically  $4.6 \mu\text{m}$ , is determined to be 4.7 dB for full  $360^\circ$  tunability at 60GHz. The aforementioned characteristics, combined with its simplicity in terms of fabrication, make the DGS-IMSL an ideal candidate for large-scale LCS.

**III-C2 RIS characterization:** Combining the presented DGS-IMSL phase shifters with antenna elements, such as patch antennas, and a biasing circuitry, an LCS can be designed. We have designed the DGS-IMSL phase shifter and the remaining components to operate around the center frequency of 60GHz. The characterization of the beamsteering capabilities of the RIS operating around 60GHz are presented in Fig. 5. The measurement setup is illustrated in Fig. 6. The RIS, with a  $4.6 \mu\text{m}$  thick LC layer, shows good beamsteering performance between  $-50^\circ$  and  $50^\circ$ .

**III-C3 Bandwidth:** The achievable  $-6$  dB bandwidth of LIQUIRIS is given in Fig. 7. With a center frequency of approximately 62 GHz LIQUIRIS features a bandwidth of 6.8 GHz, i.e. 10.9%.

**III-C4 Power consumption:** One of the key feature of LCSs is their low power consumption. To confirm this, we measure LIQUIRIS's power consumption using an E4980A Precision LCR Meter with a 1 KHz sinusoidal signal. We compute the average power consumption under the assumption of equal likelihood of all differential phases in real-world scenarios. Consequently, power consumption was evaluated across varying bias voltages (i.e., phases) and subsequently averaged. *The average power consumption of an individual delay line phase shifter in the proposed LCS-RIS is quantified at 150 nW.* Hence, for a large RIS with  $10^6$  phase shifters (corresponding to a  $5 \times 5$  m aperture for an element spacing of  $\lambda_0/2$ ), the power consumption would add up to 150 mW for LIQUIRIS. As an example for a PIN diode, the power

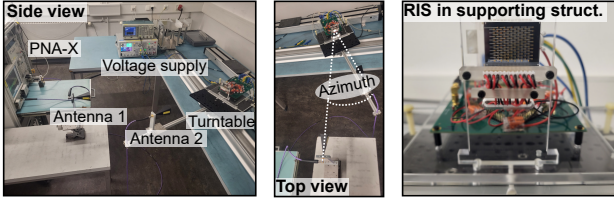


Figure 6: Bistatic measurement setup for LIQUIRIS.

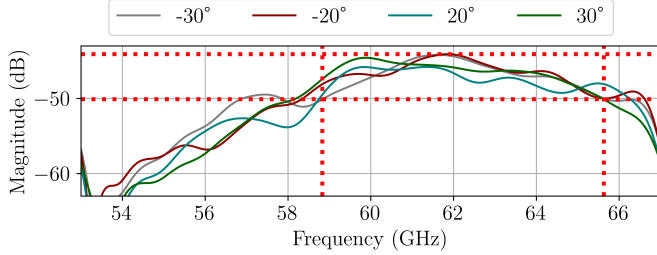


Figure 7: Measured  $-6$  dB bandwidth of LIQUIRIS for steering angles towards  $-30^\circ$ ,  $-20^\circ$ ,  $20^\circ$  and  $30^\circ$ .

consumption reported in [20] at 10.5 GHz equals 0.33 mW per diode in an on-state. Hence, a PIN diode-based RIS with  $10^6$  elements where half of the diodes are on would therefore present a 165 W, 330 W or 495 W power consumption to bias the PIN diodes in a 1-, 2-, and 3-bit configuration, respectively.

#### IV. MINIMIZING RESPONSE TIME

We consider a system consisting of a base station (BS), a set of  $L$  mobile terminals (MTs), and a planar LCS that is located in the far-field relative to the BS and MTs. The LCS is centered at location  $(0, 0)$  in the  $xz$ -plane and has  $N_x$  unit cells per row and  $N_z$  unit cells per column, making a total of  $N = N_x N_z$  unit cells. Each of the unit cells has a constant modulus and a tunable phase.

The BS has an in-built set of predefined beams, each pointing to a different angle relative to the LCS. In the event of a blockage between the BS and MTs, as depicted in Fig. 8, the BS employs one of the in-built beams to serve the MTs using the LCS as a reflector. We assume that the beam used by the BS remains fixed for some time interval  $\mathcal{T} = [t_a, t_b]$ . Since the BS serves one MT at a time, the LCS must be reconfigured at every time instant  $t_l \in \mathcal{T}$ ,  $\forall l \in \mathcal{L} = \{1, \dots, L\}$ , in order to reflect the received signals towards the  $l$ -th MT of interest.

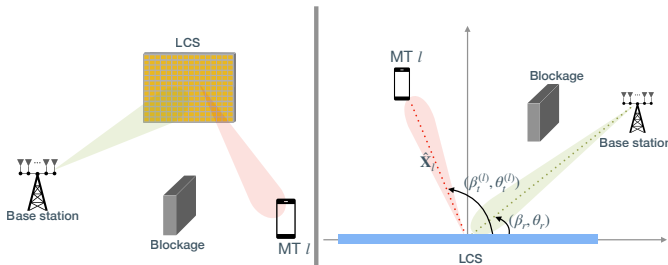


Figure 8: Overview of our system model.

Thus, for each time instant  $t_l$ , a beam  $\hat{\mathbf{x}}_l$  for the LCS is to be designed.

Assuming that the BS employs a directive antenna with gain  $G_{BS}$ , the line-of-sight (LoS) channel between the BS and the LCS is given by  $\mathbf{g} = \rho [e^{-j\frac{2\pi}{\lambda}\psi_1}, \dots, e^{-j\frac{2\pi}{\lambda}\psi_N}]^T \in \mathbb{C}^{N \times 1}$ . Specifically,  $\rho$  accounts for large-scale fading and  $\psi_n = \mathbf{v}_r^T \mathbf{p}_n$ , such that  $\mathbf{v}_r = [\sin(\theta_r) \cos(\beta_r), \sin(\theta_r) \sin(\beta_r), \cos(\theta_r)]^T \in \mathbb{R}^{3 \times 1}$  represents the phase variations of the incident signals over the LCS,  $\mathbf{p}_n \in \mathbb{R}^{3 \times 1}$  represents the Cartesian coordinates of the  $n$ -th cell, and  $n \in \mathcal{N} = \{1, \dots, N\}$ . Also,  $\beta_r$  and  $\theta_r$  denote respectively the azimuth and elevation angle of arrivals (AoAs) relative to the LCS.

Similarly, assuming that the MT uses a directive antenna with gain  $G_{MT}$ , the effective channel between the LCS and the  $l$ -th MT is denoted by  $\mathbf{h}_l$ , which assuming being a LoS channel is given by  $\mathbf{h}_l = \mu^{(l)} [e^{-j\frac{2\pi}{\lambda}\xi_1^{(l)}}, \dots, e^{-j\frac{2\pi}{\lambda}\xi_N^{(l)}}]^T \in \mathbb{C}^{N \times 1}$ , where  $\mu^{(l)}$  accounts for large-scale fading and  $\xi_n^{(l)} = \mathbf{v}_t^{(l)T} \mathbf{p}_n$ , such that  $\mathbf{v}_t^{(l)} = [\sin(\theta_t^{(l)}) \cos(\beta_t^{(l)}), \sin(\theta_t^{(l)}) \sin(\beta_t^{(l)}), \cos(\theta_t^{(l)})]^T \in \mathbb{R}^{3 \times 1}$  represents the phase variations of the reflected signals over the LCS. Additionally,  $\beta_t^{(l)}$  and  $\theta_t^{(l)}$  denote the azimuth and elevation angle of departures (AoDs) for the  $l$ -th MT, respectively.

Let the  $l$ -th beam, designed for the  $l$ -th MT, be defined as  $\hat{\mathbf{x}}_l = \delta e^{j\phi_l} \in \mathbb{C}^{N \times 1}$ , where  $\phi_l = [\phi_{l,1}, \dots, \phi_{l,N}]^T \in \mathcal{R}^{N \times 1}$  denotes the phases of the  $l$ -th beam,  $\phi_{l,n} \in \mathcal{R}$  is the  $n$ -th phase of the  $l$ -th beam,  $\mathcal{R} = [0, 2\pi)$  denotes the interval in which the phases are defined, and  $\delta$  denotes the reflection coefficient of the unit cells. Let  $P_{BS}$  denote the transmit power of the BS and  $s_l \in \mathbb{C}$  the signal transmitted from the BS to the LCS for the  $l$ -th MT, such that  $\mathbb{E}\{|s_l|^2\} = 1$ . Thus, the signal received by the  $l$ -th MT when the LCS employs beam  $\hat{\mathbf{x}}_l$  is given by

$$\begin{aligned} y_l &= \sqrt{P_{BS} G_{BS} G_{MT}} \mathbf{h}_l^H \text{diag}(\hat{\mathbf{x}}_l) \mathbf{g}^* s_l + \eta_l, \\ &= \sqrt{P_{BS} G_{BS} G_{MT}} \mathbf{h}_l^H \text{diag}(\delta e^{j\phi_l}) \mathbf{g}^* s_l + \eta_l, \\ &= \delta \sqrt{P_{BS} G_{BS} G_{MT}} \mathbf{h}_l^H \text{diag}(\mathbf{g}^*) e^{j\phi_l} s_l + \eta_l. \end{aligned}$$

The SNR of the signal at the  $l$ -th MT is defined as

$$\text{SNR}(\phi_l) = \frac{\delta^2 K^2}{\sigma^2} |\mathbf{h}_l^H \text{diag}(\mathbf{g}^*) e^{j\phi_l}|^2, \forall l \in \mathcal{L},$$

where  $K^2 = P_{BS} G_{BS} G_{MT}$  and  $\eta_l \sim (0, \sigma^2)$  symbolizes circularly symmetric Gaussian noise.

We devise two solutions for minimizing the response time of LCSs. Firstly, we formulate and solve the problem of designing the next immediate beam pattern, which we referred to as LIQUIRIS-SINGLEBEAM (see Section IV-A). Next, we extend this method to enable designing a set of beams jointly when the future AoDs are known apriori. We refer to the latter as LIQUIRIS-JOINTBEAM (see Section IV-B).

#### A. LIQUIRIS-SINGLEBEAM

To enable fast responding LCSs, we design beams that require minimal time increments when switching the service

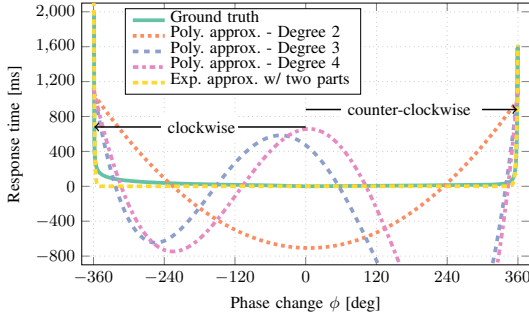


Figure 9: Different approximate functions fitted to the collected data points.

from one MT to the next. We address the response time minimization by formulating the following optimization problem,

$$\begin{aligned} \mathcal{P}_1^{(l)} : \min_{\phi_l} \quad & \bar{f}(\phi_l | \phi_{l-1}) \\ \text{s.t.} \quad & C_1 : \text{SNR}(\phi_l) \geq \alpha_l, \\ & C_2 : \phi_{l,n} \in \mathcal{R}, \forall n \in \mathcal{N}, \end{aligned}$$

which optimizes the beam for the  $l$ -th MT. In particular, the objective function  $\bar{f}(\phi_l | \phi_{l-1})$  models the response time for transitioning from the  $l-1$ -th beam, which is known, to the  $l$ -th beam that is to be designed. Additionally, constraint  $C_1$  enforces a minimum SNR threshold  $\alpha_l$  to be achieved for each MT, whereas  $C_2$  enforces the phases to be in  $\mathcal{R}$ . To serve all  $L$  MTs, the optimization problems  $\mathcal{P}_1^{(1)}$ ,  $\mathcal{P}_1^{(2)}$ ,  $\dots$ ,  $\mathcal{P}_1^{(L)}$  are solved sequentially. Problem  $\mathcal{P}_1^{(l)}$  is a nonconvex nonlinear program and is challenging to solve. We devise an algorithm based on convex optimization principles to solve  $\mathcal{P}_1^{(l)}$ . Specifically, we propose a series of steps to tame the complexities of  $\mathcal{P}_1^{(l)}$  via convexification procedures.

**IV-A1 Defining a function that relates phase change and response time:** In this section, we define a custom function that maps phase change to response time, exploiting the data already presented in Fig. 1.<sup>5</sup>

At any particular instant  $t_l$ , the unit cells must update their phases from  $\phi_{l-1}$  to  $\phi_l$  in order to switch to beam  $\hat{\mathbf{x}}_l$ . As a result, the LCS response time is dictated by the unit cell that takes the longest among all  $N$  unit cells to achieve the desired phase change. Thus, we define  $\bar{f}(\phi_l | \phi_{l-1}) = \max_{n \in \mathcal{N}} \hat{f}(\phi_{l,n} - \phi_{l-1,n})$  as the objective function, where  $\hat{f}$  characterizes the actual response time of a unit cell.

In particular, using the ground truth in its manifest form to devise function  $\hat{f}$  is impractical. One possible solution consists in finding a function fitted to the points, which can map the phase change to response time. Nevertheless, this choice may result in highly nonlinear and nonconvex functions with significant fitting errors. For instance, Fig. 9 shows functions fitted to the ground truth using polynomials of second, third, and fourth degree, which produce significant deviations and even negative values of time, which bear no physical significance. In addition, a two-part exponential function is included,

<sup>5</sup>The data shown in Fig. 1 and the data labeled as "ground truth" in Fig. 9 and Fig. 10 are the same, except that the axes have been swapped.

which more closely resembles the ground truth, but still fails to capture the correct mapping. An ideal function  $f_{\text{ideal}}$  that exactly maps each phase to the corresponding true response time is complex to devise and difficult to handle. Therefore, we propose a simple and effective approach whereby we approximate the data points using linear segments. In fact, the proposed approach is most suitable for our design since we aim to develop an algorithm based on convex optimization principles. Particularly, we construct linear segments such that a convex function  $\hat{f} : \mathcal{R} \rightarrow \mathbb{R}_+$ , which closely approximates the ideal but unknown function  $f_{\text{ideal}}$ , is obtained.

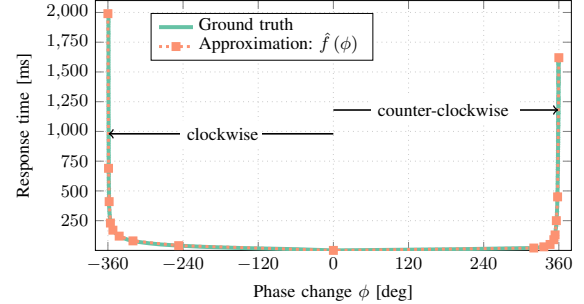


Figure 10: Ground truth and approximate response time of a unit cell.

We take  $I$  samples from the collected data points and define piecewise linear function  $\hat{f}$ , such that it is convex and consists of  $I-1$  linear segments, defined as follows

$$\hat{f}(\phi) = \begin{cases} \hat{f}_1(\phi) \triangleq a_1\phi + b_1, & \phi \in \Phi_1, \\ \vdots \\ \hat{f}_{I-1}(\phi) \triangleq a_{I-1}\phi + b_{I-1}, & \phi \in \Phi_{I-1}, \end{cases} \quad (1)$$

where  $\phi$  denotes the phase change, which can be positive (counter-clockwise direction) or negative (clockwise direction). Additionally,  $a_i \in \mathbb{R}$ , and  $b_i \in \mathbb{R}$ ,  $\forall i \in \mathcal{I}$ , denote respectively the slope and vertical shift of  $\hat{f}_i$  with respect to the origin, where  $\mathcal{I} = \{1, \dots, I-1\}$ . The slope and vertical shift of  $\hat{f}_i$  are defined as  $a_i = \frac{w_i - w_{i+1}}{c_i - c_{i+1}}$  and  $b_i = w_{i+1} - \frac{w_i - w_{i+1}}{c_i - c_{i+1}} c_{i+1}$ , such that  $c_i \in \mathbb{R}$  and  $w_i \in \mathbb{R}_+$  denote respectively the breakpoints in the abscissa and ordinate at which  $\hat{f}_i$  and  $\hat{f}_{i+1}$  intersect. Besides,  $\Phi_i = [c_i, c_{i+1}]$  represents the interval in which function  $\hat{f}_i$  prevails over other functions  $\hat{f}_{j \neq i}$ .

As shown in **Lemma 1**, we can equivalently express  $\hat{f}$  as

$$\hat{f}(\phi) = \max_{i \in \mathcal{I}} \hat{f}_i(\phi). \quad (2)$$

**Lemma 1.** Formulations (1) and (2) are equivalent for the convex piecewise linear function  $\hat{f}(\phi)$ .

*Proof.* Since  $\hat{f}$  is convex, the following inequality holds true, for  $i \in \mathcal{I}$  and  $\theta \in [0, 1]$ ,

$$\hat{f}(\theta\phi' + (1-\theta)\phi'') \leq \theta\hat{f}(\phi') + (1-\theta)\hat{f}(\phi''). \quad (3)$$

Upon reordering the terms in (3), we obtain

$$\hat{f}(\phi') \geq \hat{f}(\phi'') + \frac{\hat{f}(\phi'' + \theta(\phi' - \phi'')) - \hat{f}(\phi'')}{\theta}. \quad (4)$$

We assume that  $\phi' \in \Phi_i$  and  $\phi'' \in \Phi_j$ ,  $i, j \in \mathcal{I}$ , and choose  $\theta$  such that  $\phi^* = \phi'' + \theta(\phi' - \phi'') \in \Phi_j$ . From (1), we have

$$\begin{aligned}\hat{f}(\phi') &= \hat{f}_i(\phi') = a_i\phi' + b_i, \\ \hat{f}(\phi'') &= \hat{f}_j(\phi'') = a_j\phi'' + b_j, \\ \hat{f}(\phi^*) &= \hat{f}_j(\phi^*) = a_j\phi^* + b_j.\end{aligned}$$

Upon replacing the above relations in (4), it follows that

$$a_i\phi' + b_i \geq a_j\phi' + b_j, \phi' \in \Phi_i, \forall j \in \mathcal{I},$$

which is equivalent to

$$\begin{aligned}\hat{f}_i(\phi') &\geq \hat{f}_j(\phi'), \phi' \in \Phi_i, \forall j \in \mathcal{I}, \\ &= \max_{j \in \mathcal{I}} \hat{f}_j(\phi') = \hat{f}(\phi'), \phi' \in \Phi_i,\end{aligned}\tag{5}$$

thus completing the proof.  $\blacksquare$

The procedure proposed in this section to approximate the ground truth data points by means of a piecewise linear function is general and can be employed with any value of  $I$ . For instance, in Fig. 10 we compare the ground truth to an approximate function  $\hat{f}$  assuming  $I = 17$ .

**IV-A2 Introducing auxiliary decision variables:** We introduce auxiliary decision variables  $\gamma_{l,n} \in \mathbb{R}$  and  $\tau_l \in \mathbb{R}_+$ , which facilitate reformulating  $\mathcal{P}_1^{(l)}$ . Specifically,  $\gamma_{l,n}$  denote the argument of function  $\hat{f}$ , resulting in constraint  $C_3 : \gamma_{l,n} = \phi_{l,n} - \phi_{l-1,n}$ ,  $\forall n \in \mathcal{N}$ . In addition, we bound from above the maximum response time of the  $l$ -th beam by using nonnegative auxiliary decision variable  $\tau_l$ . Thus, we introduce constraint  $C_4 : \tau_l \geq 0$  such that  $C_5 : \max_{n \in \mathcal{N}} \hat{f}(\gamma_{l,n}) \leq \tau_l$  is satisfied, transforming the objective function into  $\tau_l$ . After considering the changes above, problem  $\mathcal{P}_1^{(l)}$  is equivalently recast as

$$\begin{aligned}\hat{\mathcal{P}}_1^{(l)} : \min_{\phi_l, \gamma_l, \tau_l} \quad & \tau_l \\ \text{s.t.} \quad & C_1 : \frac{\delta^2 K^2}{\sigma^2} |\mathbf{h}_l^H \text{diag}(\mathbf{g}^*) e^{j\phi_l}|^2 \geq \alpha_l, \\ & C_2 : \phi_{l,n} \in \mathcal{R}, \forall n \in \mathcal{N}, \\ & C_3 : \phi_{l,n} - \phi_{l-1,n} = \gamma_{l,n}, \forall n \in \mathcal{N}, \\ & C_4 : \tau_l \geq 0, \\ & C_5 : \max_{n \in \mathcal{N}} \hat{f}(\gamma_{l,n}) \leq \tau_l,\end{aligned}$$

where  $\gamma_l = [\gamma_{l,1}, \dots, \gamma_{l,N}]^T \in \mathbb{R}^{N \times 1}$ . In constraint  $C_5$ , the codomain of  $\hat{f}$  is always nonnegative, and therefore  $\max_{n \in \mathcal{N}} \hat{f}(\gamma_{l,n})$  is also nonnegative, thus making  $\tau_l$  nonnegative by default. As a result,  $C_4$  can be dropped as  $C_5$  ensures that  $\tau_l \geq 0$ .

By employing (2), constraint  $C_5$  can be recast as  $\max_{n \in \mathcal{N}} \max_{i \in \mathcal{I}} \hat{f}_i(\gamma_{l,n}) \leq \tau_l$ , which is equivalent to

$$C_6 : \hat{f}_i(\gamma_{l,n}) \leq \tau_l, \forall n \in \mathcal{N}, i \in \mathcal{I}.$$

Thus, problem  $\hat{\mathcal{P}}_1^{(l)}$  is equivalently transformed into

$$\tilde{\mathcal{P}}_1^{(l)} : \min_{\phi_l, \gamma_l, \tau_l} \tau_l \text{ s.t. } C_1, C_2, C_3, C_6.$$

**REMARK:** The objective of  $\tilde{\mathcal{P}}_1^{(l)}$  and constraints  $C_2, C_3$ , and  $C_6$  are convex whereas constraint  $C_1$  is nonconvex, which is addressed in Section IV-A3 and Section IV-A4.

**IV-A3 Transforming phase selection into multiple linear constraints:** Term  $e^{j\phi_l}$  in constraint  $C_1$  complicates the direct optimization of decision variables  $\phi_{l,n}$  since the latter are the arguments of complex exponential functions. Instead of considering  $\phi_{l,n}$  as the decision variables, we resort to optimizing  $e^{j\phi_{l,n}}$ , which dwell in the unit circumference. To this end, we introduce decision variables  $\mathbf{x}_l = [x_{l,1}, \dots, x_{l,N}]^T \in \mathcal{S}^{N \times 1}$ , where  $\mathcal{S} = \left\{1, e^{j\frac{2\pi}{Q}}, \dots, e^{j\frac{2\pi(Q-1)}{Q}}\right\}$  is the set of admissible phases uniformly spaced in the unit circumference<sup>6</sup> and  $Q = |\mathcal{S}|$  is the cardinality of set  $\mathcal{S}$ , such that  $\mathbf{x}_l$  replaces  $e^{j\phi_l}$  in  $C_1$ . Replacing  $e^{j\phi_l}$  with  $\mathbf{x}_l$  removes the complication of optimizing  $\phi_l$  in  $C_1$  but affects constraints  $C_2$  and  $C_3$ . Therefore, for a discrete set of phase shifts  $\mathcal{S}$ , constraints  $C_1, C_2$ , and  $C_3$  are transformed into  $C_7, C_8, C_9, C_{10}$ , and  $C_{11}$ , as shown in the following:

$$C_1, C_2, C_3 \Leftrightarrow \begin{cases} C_7 : \frac{\delta^2 K^2}{\sigma^2} |\mathbf{h}_l^H \text{diag}(\mathbf{g}^*) \mathbf{x}_l|^2 \geq \alpha_l, \\ C_8 : z_{l,n,q} \in \{0, 1\}, \forall n \in \mathcal{N}, q \in \mathcal{Q}, \\ C_9 : \mathbf{1}^T \mathbf{z}_{l,n} = 1, \forall n \in \mathcal{N}, \\ C_{10} : x_{l,n} = \mathbf{s}^T \mathbf{z}_{l,n}, \forall n \in \mathcal{N}, \\ C_{11} : \underline{x}_{l,n} - \underline{x}_{l-1,n} = \gamma_{l,n}, \forall n \in \mathcal{N}. \end{cases}$$

Specifically,  $\mathbf{s} \in \mathcal{S}^{Q \times 1}$  contains all the elements in  $\mathcal{S}$ , i.e.,  $\mathbf{s} = \left[1, e^{j\frac{2\pi}{Q}}, \dots, e^{j\frac{2\pi(Q-1)}{Q}}\right]^T$ , and  $\mathcal{Q} = \{1, \dots, Q\}$ . Constraint  $C_7$  is obtained by simply replacing  $e^{j\phi_l}$  with  $\mathbf{x}_l$ . Constraint  $C_8$  enforces all elements of vector  $\mathbf{z}_{l,n}$  to be binary. Constraint  $C_9$  enforces only one element of vector  $\mathbf{z}_{l,n}$  to be 1. Thus,  $C_{10}$  has the effect of making each  $x_{l,n}$  take one value from  $\mathcal{S}$ . Operator  $\underline{x}_{l,n}$  in constraint  $C_{11}$  extracts the phase of  $x_{l,n}$  in degrees, and therefore  $C_{11}$  is equivalent to  $C_3$ .

The phase operator is nonlinear as it is defined as  $\underline{x}_{l,n} = \arctan\left(\frac{\text{Im}(x_{l,n})}{\text{Re}(x_{l,n})}\right)$ , which is difficult to deal with. Conventional approaches linearize  $\arctan(x_{l,n})$  with respect to  $x_{l,n}$  to circumvent the nonlinearity. However, linearization leads to additional hindrances, such as choosing a suitable initialization for  $x_{l,n}$  and the need for multiple iterations to improve the solution. To cope with the phase operator in  $C_{11}$ , we propose the following strategy. We introduce vector  $\mathbf{r}$  defined as  $\mathbf{r} = \underline{\mathbf{s}} = \left[0, \frac{360}{Q}, \dots, \frac{360(Q-1)}{Q}\right]$ , i.e., it contains the phases of set  $\mathcal{S}$  in degrees. By ensuring that there is one-to-one correspondence between the elements of  $\mathbf{r}$  and  $\mathbf{s}$ , i.e.,  $r_q = \underline{s}_q$ , we take advantage of constraints  $C_8, C_9$ , and  $C_{10}$  to express  $\underline{x}_{l,n} = \mathbf{r}^T \mathbf{z}_{l,n}$ . As a result,  $C_{11}$  can be equivalently recast as

$$C_{12} : \mathbf{r}^T \mathbf{z}_{l,n} - \mathbf{r}^T \mathbf{z}_{l-1,n} = \gamma_{l,n}, \forall n \in \mathcal{N}.$$

After the proposed changes,  $\tilde{\mathcal{P}}_1^{(l)}$  is transformed into  $\bar{\mathcal{P}}_1^{(l)}$

$$\bar{\mathcal{P}}_1^{(l)} : \min_{\mathbf{x}_l, \mathbf{z}_l, \gamma_l, \tau_l} \tau_l \text{ s.t. } C_6, C_7, C_8, C_9, C_{10}, C_{12},$$

<sup>6</sup>Note that for LCSs, a high phase-shift resolution is affordable. With the proposed formulation, this capability of LCSs is translated into assuming a large  $Q$ , e.g., we adopt  $Q = 256$  in our LCS testbed.

where  $\mathbf{Z}_l = [\mathbf{z}_{l,1}, \dots, \mathbf{z}_{l,N}] \in \{0, 1\}^{Q \times N}$  collects all variables  $\mathbf{z}_{l,n}$ ,  $\forall n \in \mathcal{N}$ .

REMARK: All constraints except  $C_7$  are convex. In the following, we deal with the convexification of  $C_7$ .

**IV-A4 Convexifying nonconvex constraints:** One possibility to deal with nonconvex constraint  $C_7$  is to linearize it with respect to  $\mathbf{x}_l$  and iteratively refine the solution. However, we adopt a different strategy whereby we replace it by an inner convex approximation of  $C_7$ , relying on **Lemma 2**.

**Lemma 2.** *Nonconvex constraint  $|y| \geq a$ , where  $y \in \mathbb{C}$  is a decision variable and  $a \in \mathbb{R}$  is a scalar, is ensured by default if convex constraint  $\text{Re}\{y\} \geq a$  is satisfied. Particularly, the latter is a convex inner approximation of the former as it has a more constrained feasible set.*

*Proof.* Recall that  $|y| = \sqrt{\text{Re}\{y\}^2 + \text{Im}\{y\}^2}$ . If  $\text{Re}\{y\} \geq a$  holds true, then  $|y| \geq a$  is automatically satisfied since  $\text{Re}\{y\} \geq a$  is more constrained than  $|y| \geq a$ . The inequality  $|y| \geq \text{Re}\{y\}$  becomes tight when the phase of  $y$  is zero. ■

Constraint  $C_7$  is equivalent to  $\frac{\delta K}{\sigma} |\mathbf{h}_l^H \text{diag}(\mathbf{g}^*) \mathbf{x}_l| \geq \sqrt{\alpha_l}$  after taking the square root on both sides. Now, invoking **Lemma 2**, constraint  $C_7$  is enforced if  $C_{13} : \frac{\delta K}{\sigma} \text{Re}\{\mathbf{h}_l^H \text{diag}(\mathbf{g}^*) \mathbf{x}_l\} \geq \sqrt{\alpha_l}$ . Therefore,  $\tilde{\mathcal{P}}_1^{(l)}$  is transformed into

$$\tilde{\mathcal{P}}_1^{(l)} : \min_{\mathbf{x}_l, \mathbf{Z}_l, \gamma_l, \tau_l} \tau_l \text{ s.t. } C_6, C_8, C_9, C_{10}, C_{12}, C_{13}.$$

REMARK: The feasible set enforced by  $C_{13}$  is within the original feasible set induced by  $C_7$ . Therefore, the solution to  $\tilde{\mathcal{P}}_1^{(l)}$  is also a feasible solution to  $\bar{\mathcal{P}}_1^{(l)}$ , however, due to the reduced feasible set in  $\bar{\mathcal{P}}_1^{(l)}$ , it is not guaranteed that both problems have the same optimal solution.

**IV-A5 Computational complexity:** Decision variables  $\mathbf{x}_l$  and  $\gamma_l$  depend only on  $\mathbf{Z}_l$ . Therefore, they can be omitted from  $\tilde{\mathcal{P}}_1^{(l)}$  by directly using the definitions in  $C_{10}$  and  $C_{12}$ , reducing the number of the decision variables, the number of constraints, and subsequently the computational complexity. In particular,  $\tilde{\mathcal{P}}_1^{(l)}$  can be recast as

$$\begin{aligned} \tilde{\mathcal{P}}_1^{(l)} : \min_{\mathbf{Z}_l, \tau_l} \quad & \tau_l \\ \text{s.t.} \quad & C_6 : \hat{f}_i(\mathbf{r}^T \mathbf{z}_{l,n} - \mathbf{r}^T \mathbf{z}_{l-1,n}) \leq \tau_l, \\ & \forall n \in \mathcal{N}, i \in \mathcal{I}, \\ & C_8 : z_{l,n,q} \in \{0, 1\}, \forall n \in \mathcal{N}, q \in \mathcal{Q}, \\ & C_9 : \mathbf{1}^T \mathbf{z}_{l,n} = 1, \forall n \in \mathcal{N}, \\ & C_{13} : \frac{\delta K}{\sigma} \text{Re}\{\mathbf{h}_l^H \text{diag}(\mathbf{g}^*) \mathbf{Z}_l^T \mathbf{s}\} \geq \sqrt{\alpha_l}. \end{aligned}$$

After solving  $\tilde{\mathcal{P}}_1^{(l)}$ , we compute the  $l$ -th beam as  $\mathbf{x}_l = \delta \mathbf{Z}_l^T \mathbf{s}$ . Specifically, problem  $\tilde{\mathcal{P}}_1^{(l)}$  is a mixed binary linear programming problem. Although the worst-case complexity of  $\tilde{\mathcal{P}}_1^{(l)}$  is combinatorial, i.e.,  $\mathcal{O}(Q^N)$ , many schemes have been developed in the literature to obtain efficient low-complexity solutions, e.g., based on binary relaxation with non-binary value penalization [21]. Problem  $\tilde{\mathcal{P}}_1^{(l)}$  can be efficiently solved using established and well-known solvers such as MOSEK.

## B. LIQUIRIS-JOINTBEAM

Our first proposed approach provides optimized phase shift configurations to transition from one arbitrary beam to another. In LIQUIRIS-JOINTBEAM, we devise beamforming solutions for scenarios where the initial standard-defined beam training is completed, i.e., transmitter knows AoDs. This is a reasonable assumption in 5G NR since the transmitter performs regular beams sweeps per standard definition.

Following the same procedure as in Section IV-A, we define problem  $\tilde{\mathcal{P}}_2$ , which co-designs  $L$  beams jointly, each for a different MT, accounting for the overall response time needed to switch to each of the  $L$  beams in a sequential manner, i.e., from  $\mathbf{x}_1$  to  $\mathbf{x}_2$ , from  $\mathbf{x}_2$  to  $\mathbf{x}_3$ , and so on.

$$\begin{aligned} \tilde{\mathcal{P}}_2 : \min_{\mathbf{Z}, \tau} \quad & \sum_{l \in \mathcal{L}} \tau_l \\ \text{s.t.} \quad & C_6 : \hat{f}_i(\mathbf{r}^T \mathbf{z}_{l,n} - \mathbf{r}^T \mathbf{z}_{l-1,n}) \leq \tau_l, \\ & \forall l \in \mathcal{L}, n \in \mathcal{N}, i \in \mathcal{I}, \\ & C_8 : z_{l,n,q} \in \{0, 1\}, \forall l \in \mathcal{L}, n \in \mathcal{N}, q \in \mathcal{Q}, \\ & C_9 : \mathbf{1}^T \mathbf{z}_{l,n} = 1, \forall l \in \mathcal{L}, n \in \mathcal{N}, \\ & C_{13} : \frac{\delta K}{\sigma} \text{Re}\{\mathbf{h}_l^H \text{diag}(\mathbf{g}^*) \mathbf{Z}_l^T \mathbf{s}\} \geq \sqrt{\alpha_l}, \forall l \in \mathcal{L}. \end{aligned}$$

In  $\tilde{\mathcal{P}}_2$ ,  $\mathbf{Z}$  represents the collection of all  $\mathbf{Z}_l$  and  $\tau = [\tau_1, \dots, \tau_L]^T$ .  $\tilde{\mathcal{P}}_2$  is also a mixed binary linear program that can be solved efficiently using commercial solvers. A particular difference with respect to  $\tilde{\mathcal{P}}_1^{(l)}$  is that the number of decision variables in  $\tilde{\mathcal{P}}_2$  is  $L$  times that of  $\tilde{\mathcal{P}}_1^{(l)}$ , and is therefore more complex to solve. However,  $\tilde{\mathcal{P}}_2$  can bring additional response time reductions, as shown in Section V.

## V. EVALUATION

In this section, we evaluate and analyze LIQUIRIS using our 60GHz LCS prototype.

**Benchmark.** To paint a clearer picture of LIQUIRIS, we compare our proposed solution with the so-called LEGACY method, which designs beams to maximize the SNR for each of the  $L$  MTs without accounting for the time incurred due to phase change. It is defined as

$$\begin{aligned} \tilde{\mathcal{P}}_3 : \max_{\mathbf{Z}, \alpha} \quad & \sum_{l \in \mathcal{L}} \alpha_l \\ & C_8 : z_{l,n,q} \in \{0, 1\}, \forall l \in \mathcal{L}, n \in \mathcal{N}, q \in \mathcal{Q}, \\ & C_9 : \mathbf{1}^T \mathbf{z}_{l,n} = 1, \forall l \in \mathcal{L}, n \in \mathcal{N}, \\ & C_{13} : \frac{\delta K}{\sigma} \text{Re}\{\mathbf{h}_l^H \text{diag}(\mathbf{g}^*) \mathbf{Z}_l^T \mathbf{s}\} \geq \alpha_l, \end{aligned}$$

where  $\alpha = [\alpha_1, \dots, \alpha_L]^T$ . Unlike  $\tilde{\mathcal{P}}_2$  in which the current beam influences the optimization of the next beam,  $\tilde{\mathcal{P}}_3$  is not subject to such a condition. The beams in  $\tilde{\mathcal{P}}_3$  can be obtained via a simultaneous or sequential solution, leading to the same result since the beams are independent of each other.

**Performance metric.** For our evaluation, we chose to demonstrate: (i) Beam pattern. LIQUIRIS employs a different method for computing the beamforming vector<sup>7</sup>, which is more restrictive than the LEGACY method. We choose to

<sup>7</sup>We assume the initial phases at  $l = 0$  are zero, i.e.,  $\mathbf{x}_0 = [1, \dots, 1]^T$ .



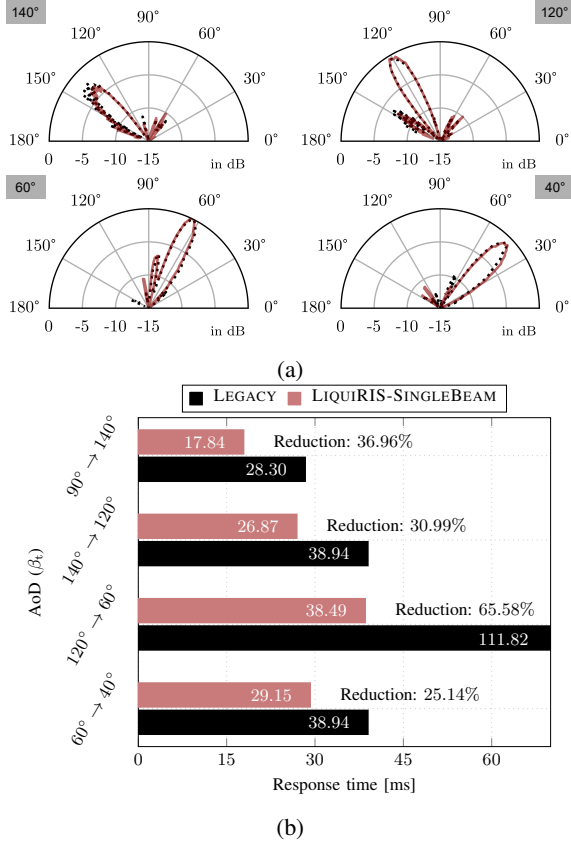


Figure 11: The response time incurred under LIQUIRIS-SINGLEBEAM and LEGACY. Our proposed solution results in a much lower response time (by up to 65.5%) while maintaining the same beam pattern.

know the resulting beam pattern, instead of averaged/peak power/SNR valued to provide a deeper insight on the impact of our proposal in real system performance; (ii) Response time. LIQUIRIS aims at reducing the response time of beam switching at LCSs. Therefore, we also compute and show the response time needed for achieving the desired beam<sup>8</sup>.

#### A. Experimental setup

Our LCS consists of 120 radiating elements arranged in a rectangular grid in 12 columns and 10 rows. Each reflecting element of the LCS is coupled to a distinct phase shifter. The fabricated LCS is capable of beam steering in one plane as we have only enabled biasing in columns such that all elements in one column experience the same applied voltage and, as a result, the same phase shift. However, it has to be noted that element-wise biasing (and hence, 3D beam steering capabilities) is only a technological challenge already solved for modern LC displays.

Our measurement setup, as shown in Fig. 6, includes Two MI-Wave V-Band horn antennas with 25 dBi gain pointing towards the LCS. Antennas 1 and 2 have a distance of

<sup>8</sup>The response times are computed using the response time of individual phase shifters as shown and characterized in Fig. 10.

approximately 1 m and 60 cm to the LCS. Antenna 2 co-rotates with the turntable on which the LCS is placed. The antennas are connected to a PNA-X N5247A from Keysight Technologies. The LCS is biased with a DAC60096 EVM generating a 1 kHz square wave signal. In order to isolate the response of the LCS from the cluttered environment, two reference measurements are taken, and time gating is applied.

#### B. Performance of LIQUIRIS-SINGLEBEAM

In this scenario, we evaluate the performance of LIQUIRIS-SINGLEBEAM compared to the LEGACY method. Specifically, we show the achieved beam patterns for a diverse set of AoDs, i.e.,  $\{140^\circ, 120^\circ, 60^\circ, 40^\circ\}$ , and their corresponding response time.

In Fig. 11a, we observe that LIQUIRIS-SINGLEBEAM produces beam patterns that are very similar to that of the LEGACY method. This figure demonstrates that: (i) our proposed approach achieves nearly the same gain as the LEGACY method on the main-lobe and (ii) the overall beam pattern on both side- and main-lobes are very similar, confirming that our proposed method does not result in unwanted radiation/interference in other directions. Observing the results in Fig. 11b, we note that LIQUIRIS-SINGLEBEAM reduces the response time on average by 39.67%, with a maximum of 65.58% when transitioning from 120° to 60°, and a minimum of 25.14% when transitioning from 60° to 40°<sup>9</sup>.

#### C. Performance of LIQUIRIS-JOINTBEAM

In this scenario, we evaluate the performance of LIQUIRIS-JOINTBEAM against the LEGACY method. Unlike the previous scenario, here, LIQUIRIS-JOINTBEAM designs the beams for four AoDs jointly, accounting for the overall response time of all phase transitions. This is analogous to a scenario in which an LCS intends to serve four MTs sequentially, located in the directions  $\{135^\circ, 115^\circ, 65^\circ, 45^\circ\}$ . To this aim, LIQUIRIS-JOINTBEAM designs the four beams such that the response time for transitioning  $90^\circ \rightarrow 135^\circ \rightarrow 115^\circ \rightarrow 65^\circ \rightarrow 45^\circ$  is minimized.

Fig. 12a illustrates the achieved beam patterns and the response time with LIQUIRIS-JOINTBEAM and the LEGACY method. We observe in this figure that the beam pattern produced by our proposed approach is very similar to that of LEGACY. At the same time, our proposed approach achieves a much lower response time compared to the LEGACY method, see Fig. 12b. More specifically, as we transition among these four beams, LIQUIRIS-JOINTBEAM incurred on average 34.19% lower response time.

#### D. Impact of angular separation

In this scenario, we examine the performance of all approaches under different angular separations. Specifically, we investigate a scenario with three desired AoDs (e.g., three MTs at different locations) where the angular separations are  $5^\circ$ ,  $10^\circ$ ,  $15^\circ$ , and  $30^\circ$ .

<sup>9</sup>The starting angle is  $90^\circ$  because the transmitter is exactly in front of the LCS, i.e.,  $\beta_T = 90^\circ$ , and the initial phases at  $l = 0$  are  $\mathbf{x}_0 = [1, \dots, 1]^T$ .

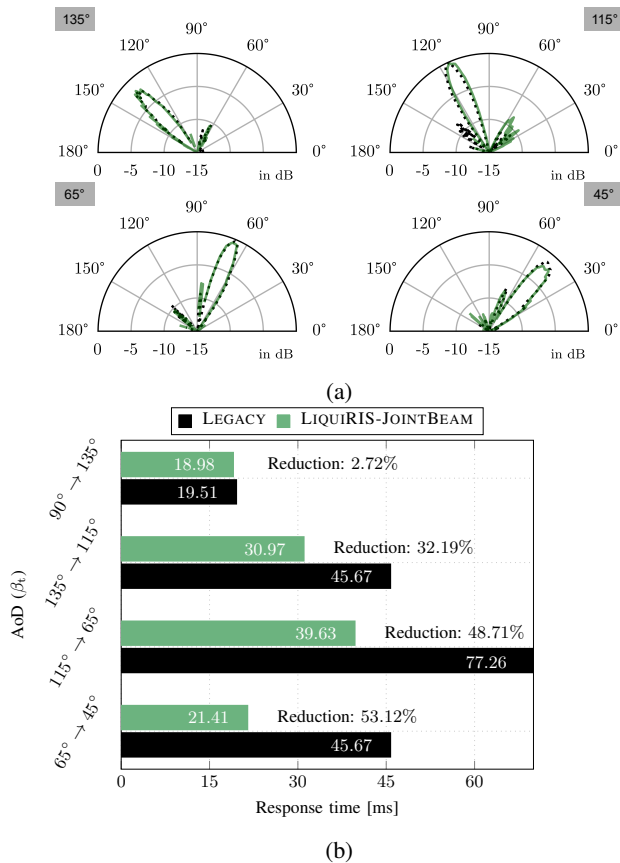


Figure 12: The response time incurred under LIQUIRIS-JOINTBEAM and LEGACY. *Our proposed solution reduces the response time by up to 53.1%*

In Fig. 13a, we observe that both LIQUIRIS-SINGLEBEAM and LIQUIRIS-JOINTBEAM shape a beam pattern very similar to that of LEGACY. In terms of response time, LIQUIRIS significantly outperforms LEGACY; see Fig. 13b. The response times also illustrate that LIQUIRIS consistently outperforms LEGACY independently of the angular separation. Furthermore, we observe that LIQUIRIS-JOINTBEAM, on average, achieves 8.41% lower response time compared to LIQUIRIS-SINGLEBEAM. This is due to the fact that LIQUIRIS-SINGLEBEAM designs the beams under more constrained conditions as it always depends on the currently used beam. In contrast, LIQUIRIS-JOINTBEAM has more freedom for the beams design, and can account for the global phase changes on all beams to be designed, thus accomplishing a shorter overall response time.

#### E. Advantage of LIQUIRIS-JOINTBEAM over LIQUIRIS-SINGLEBEAM

As shown in Section V-D, the advantage of LIQUIRIS-JOINTBEAM over LIQUIRIS-SINGLEBEAM was in the order of 8 – 9%, which does not represent a substantial gain. However, in Section V-D, we only considered the design of four beams. Here, we compare the two approaches assuming an angular separation of  $5^\circ$  for a wider range of number of beams, i.e., from  $L = 1$  to  $L = 10$ , which is shown in Fig. 14.

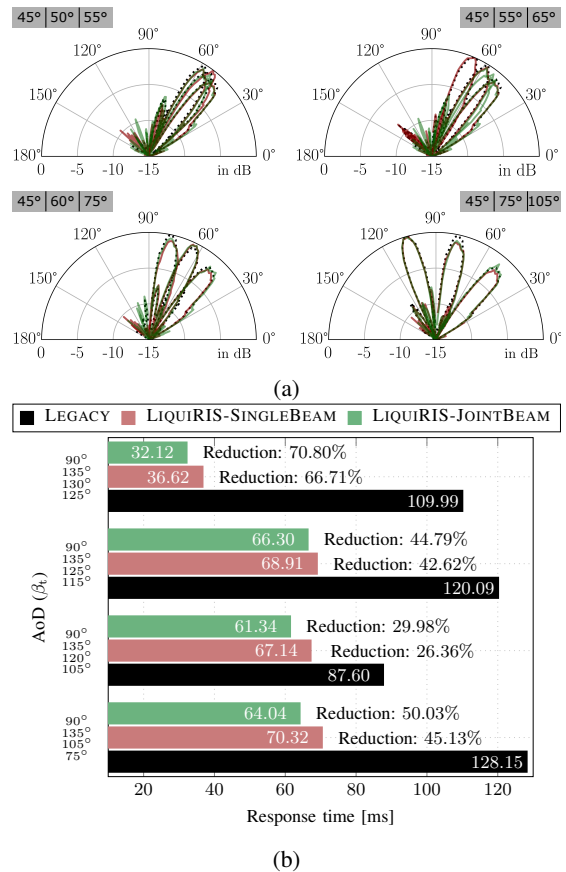


Figure 13: Analyzing the impact of angular separation on LIQUIRIS. The experiment illustrates that LEGACY is outperformed by LIQUIRIS-SINGLEBEAM and LIQUIRIS-JOINTBEAM by up to 66.71% and 70.80%, respectively.

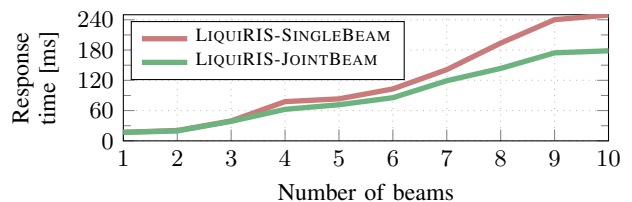


Figure 14: Response time as a function of the number of beams.

In particular, a noticeable performance difference between the two methods becomes apparent when the number of beams is large. Specifically, LIQUIRIS-JOINTBEAM is 28.39% faster than LIQUIRIS-SINGLEBEAM when the number of beams is 10. Thus, LIQUIRIS-SINGLEBEAM can be used when the number of beams is relatively small since it is less complex in its solution than LIQUIRIS-JOINTBEAM. In contrast, LIQUIRIS-JOINTBEAM is preferable when the number of beams to be designed is relatively large since only then can gains be obtained, for which it is worth facing a higher computational complexity.

### F. A deeper look into response times

So far we evaluated the response time for a limited set of AoDs. To shed light on the overall impact of LIQUIRIS on the response time, we have designed a set of 9261 beams with different AoAs and AoDs. Specifically, analyzing a large number of beams designed for a wide range of directions allows us to get a clearer picture of the response times. In Fig. 15, we demonstrate the response times under LIQUIRIS-SINGLEBEAM and the LEGACY method. The figure confirms that designing beams using LIQUIRIS-SINGLEBEAM generally results in much lower response times, on average 68.98% lower than LEGACY. The histograms in Fig. 15a and Fig. 15b show that LIQUIRIS-SINGLEBEAM exhibits a bounded response time that does not exceed 41 ms, while the LEGACY method has a response time that can extend beyond 400 ms and has a very long tail that raises uncertainty to the time required for beam switching. The cumulative distribution functions (CDFs) in Fig. 15c and Fig. 15d show that approximately 95% of the beams designed with LIQUIRIS-SINGLEBEAM incur in 30 ms or less delay whereas only 26% of the beams designed with the LEGACY method falls within this response time range.

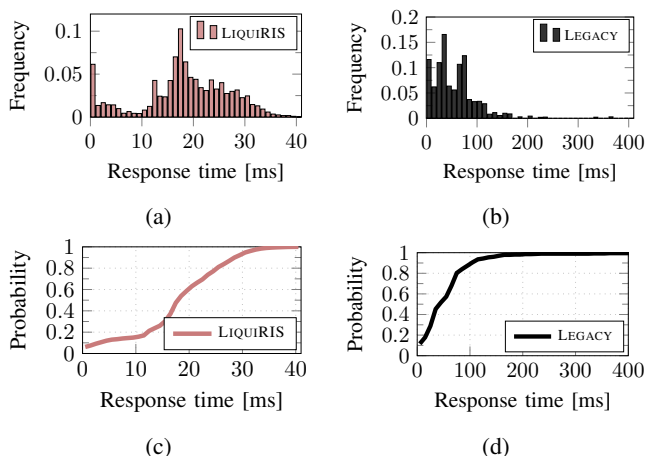


Figure 15: Histograms and CDFs of LIQUIRIS-SINGLEBEAM and LEGACY.

## VI. DISCUSSION

### A. Cost of LCS

In contrast to semiconductor-based RISs, which necessitate a minimum of one diode per Unit Cell, LCSs can be constructed in a more cost-effective manner. Leveraging the established proficiency in LCD manufacturing, large-scale RISs can be produced efficiently in substantial quantities. Given the low thickness of LCS, the cost of liquid crystal is significantly reduced in comparison to thicker LC layers [6]. For instance, the amount of liquid crystal required for a five  $\mu\text{m}$  RIS would be 20 times smaller than that needed for a 100  $\mu\text{m}$  LCS. Similarly, the currently used gold plating is 2  $\mu\text{m}$  thick and therefore does not substantially contribute to the cost of the prototype. Adding those costs to the small glass material (AF 32 ECO from Schott AG), we estimate a material

cost-per-prototype close to \$100. This cost is mainly affected by the small quantities acquired (LCS, glass) and the in-house metalization process (use of gold instead of copper) and would become exponentially lower for high quantities.

### B. Impact of quantization

As mentioned in Section IV, we quantize the phases considering  $Q = 256$ , roughly giving an angular resolution of  $1.4^\circ$ .

To evaluate how our proposed approach is influenced by quantization, we devise a scenario with different quantization levels, i.e.,  $Q = \{32, 64, 128, 1024\}$ , which is shown in Fig. 16. We consider a single MT and employ LIQUIRIS-SINGLEBEAM assuming that the AoA is  $\beta_r = 45^\circ$  and the AoD is  $\beta_t = \{91^\circ, 92^\circ, \dots, 179^\circ\}$ . Due to specular reflection, the phases of the LCS (which are initially assumed to be zero) do not need any change when  $\beta_t = 135^\circ$ , and therefore, the response time incurred by LIQUIRIS-SINGLEBEAM is zero for this specific case. Furthermore, we note that our approach is robust to the choice of quantization levels since the performance is almost the same for all values of  $Q$ .

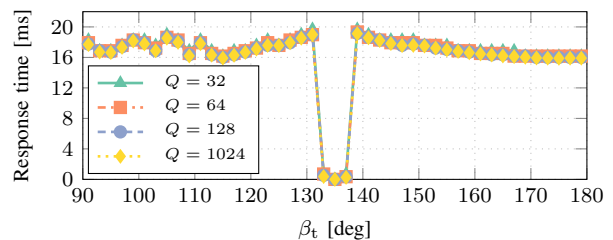


Figure 16: Response time of LIQUIRIS-SINGLEBEAM.

### C. Use-cases

We believe that LCSs are a promising solution to realize a cost-effective scalable RIS in practice. In fact, the commercial fabrication of LC-RISs can be based on the standard LC Display (LCD) technology. Despite the admittedly slower response time of LCSs, we do believe that there are various application scenarios where LCSs are viable options. Furthermore, in LIQUIRIS we broaden their use-cases in wireless network by going beyond static scenarios. For instance, the required response-time for an LCS with  $3^\circ$  beamwidth serving a user moving at 5km/h at a 5m distance (indoor) is  $192\text{ms}^{10}$ . This requirement is 37ms for an alternative outdoor scenario (100km/h, 20m,  $3^\circ$  beamwidth), which is comparable with our results (see Section V).

## VII. RELATED WORKS

To date, several technologies have been investigated in the literature for the experimental realization of phase-shifting components of RISs among which PIN diodes, varactor diodes, MEMS switches, and liquid crystals have attracted

<sup>10</sup>Response time [s]=beamwidth [rad]  $\times$  distance [m]/speed [m/s]

Table I: Comparison among different RIS designs

	Tuning time	Tunability	Power consumption
PIN diode	ns	discrete (1 bit/diode)	medium
Varactor	ns	continuous	medium
MEMS	1 – 100s of $\mu$	discrete	low
LC	> 10 ms	continuous	low

more attention [22] and hence will be reviewed in the following. We also provide an overview of their key features in Table I.

**PIN diode-based RIS experimental work:** A PIN diode is a low-capacitance device with high-frequency switching capabilities. By toggling between low and high-resistance states of multiple PIN diodes, one of several states with distinct phase-shifting properties can be activated. PIN diodes have been widely used in RIS designs [3], [9], [23], [24], [25]. These experimental setups cover both sub-6 GHz bands [3], [23], [24] and mmWave bands (mainly 28 GHz) [3], [9], [25]. Moreover, due to the inherent discreteness of phase shifts realized by PIN diodes, they often offer only a few-bit phase-shift resolution, e.g., one bit in [24] or two bits in [3], [23].

**Varactor diode-based RIS experimental work:** Varactor diodes are special diodes that can provide variable capacitance with changing voltage, which can then be used to continuously modulate the phase shift applied by the RIS unit cell. Varactors are mainly used in the design of sub-6 GHz RISs [14], [13] since their high capacitance limits their maximum operation frequency. Nonetheless, varactor-based RIS designs for mmWave bands have also been reported in the literature, see, e.g., [26] for a varactor-based RIS design at 24.5 GHz.

**MEMS-based RIS experimental work:** At higher frequencies (above 30 GHz), PIN and varactor diodes show high insertion losses. For high-frequency bands, MEMS and LC are promising technologies for realizing RISs. While over the last decades, various MEMS-based meta-surfaces have been developed [27], their main application focus has not been on improving the wireless channel. Moreover, MEMS-based RISs are mainly suitable for THz bands and not the mmWave band, which is the focus of this paper. Furthermore, *MEMS and in general mechanical-type switches are subject to failures due to aging of moving parts over time* [22].

**LCS experimental work:** Recently, a few publications have shown the use of LC for the realization of digital metasurfaces [28]. For instance, [29] presents the realization of an LCS with 1-bit programmable elements. Similarly, a 1-bit design at 0.645 THz is presented in [30] for transmissive RISs. In this case, 1-bit, two-column-wise biasing is realized, so that an array of  $64 \times 64$  elements is controlled with 32 electrodes and the ground plane as a common electrode. The designs in [29], [30] follow the reflectarray implementation. In [31], initial works for realizing an LCS following the phased-array implementation have been reported.

**Optimization method:** In the RIS literature, which is mainly based on PIN diodes, there has been extensive research on phase shift designs considering different goals. For example, [32], [33], [34] studied the phase shift design

to enhance rate fairness, while [35], [36], [37] focused on maximizing the sum-rate. In addition, other studies have explored designs aimed at maximizing energy efficiency [38], [39], [40] and minimizing transmit power [41], [42], [43]. Compared to the existing approaches, LIQUIRIS introduces a novel design objective previously unexplored, i.e., minimizing beam response time. Specifically, this aspect is inherent to liquid crystal surfaces and opens a new avenue of research in this field.

## VIII. CONCLUSION

LIQUIRIS bring cost-effective RIS tech a step closer to large deployment by introducing novel LCS design couple with physics-informed beamforming optimization schemes that can significantly reduce the response time of the LCSs, promising efficient RIS integration in wireless systems, though further research is needed.

## REFERENCES

- [1] L. Yezhen *et al.*, "A novel 28 ghz phased array antenna for 5g mobile communications," *ZTE Communications*, vol. 18, no. 3, pp. 20–25, 2020.
- [2] G. Trichopoulos *et al.*, "Design and evaluation of reconfigurable intelligent surfaces in real-world environment," *arXiv preprint arXiv:2109.07763*, 2021.
- [3] L. Dai *et al.*, "Reconfigurable intelligent surface-based wireless communications: Antenna design, prototyping, and experimental results," *IEEE Access*, vol. 8, pp. 45 913–45 923, 2020.
- [4] J. Hu *et al.*, "Reconfigurable intelligent surface based rf sensing: Design, optimization, and implementation," *IEEE Journal on Selected Areas in Communications*, vol. 38, no. 11, pp. 2700–2716, 2020.
- [5] R. Fara *et al.*, "A prototype of reconfigurable intelligent surface with continuous control of the reflection phase," *arXiv preprint arXiv:2105.11862*, 2021.
- [6] V. Arun and H. Balakrishnan, "Rfoc: Beamforming using thousands of passive antennas," in *USENIX NSDI*, 2020.
- [7] M. Dunna *et al.*, "Scattermimo: Enabling virtual mimo with smart surfaces," in *ACM MobiCom*, 2020.
- [8] M. Rossanese, P. Mursia, A. Garcia-Saavedra, V. Sciancalepore, A. Asadi, and X. Costa-Perez, "Designing, building, and characterizing RF switch-based reconfigurable intelligent surfaces," pp. 69–76, 2022.
- [9] J.-B. Gros, V. Popov, M. A. Odit, V. Lenets, and G. Lerosey, "A reconfigurable intelligent surface at mmwave based on a binary phase tunable metasurface," *IEEE Open Journal of the Communications Society*, vol. 2, pp. 1055–1064, 2021.
- [10] X. Tan, Z. Sun, D. Koutsonikolas, and J. M. Jornet, "Enabling indoor mobile millimeter-wave networks based on smart reflect-arrays," in *IEEE INFOCOM 2018-IEEE Conference on Computer Communications*. IEEE, 2018, pp. 270–278.
- [11] X. Zeng, Q. Hu, C. Mao, H. Yang, Q. Wu, J. Tang, X. L. Zhao, and X. Y. Zhang, "High-accuracy reconfigurable intelligent surface using independently controllable methods," in *2021 IEEE International Workshop on Electromagnetics: Applications and Student Innovation Competition (iWEM)*. IEEE, 2021, pp. 1–3.
- [12] M. M. Amri, N. M. Tran, and K. W. Choi, "Reconfigurable intelligent surface-aided wireless communications: Adaptive beamforming and experimental validations," *IEEE Access*, vol. 9, pp. 147 442–147 457, 2021.
- [13] X. Pei, H. Yin, L. Tan, L. Cao, Z. Li, K. Wang, K. Zhang, and E. Björnson, "Ris-aided wireless communications: Prototyping, adaptive beamforming, and indoor/outdoor field trials," *IEEE Transactions on Communications*, vol. 69, no. 12, pp. 8627–8640, 2021.
- [14] A. Araghi, M. Khalily, M. Safaei, A. Bagheri, V. Singh, F. Wang, and R. Tafazolli, "Reconfigurable intelligent surface (RIS) in the sub-6 GHz band: Design, implementation, and real-world demonstration," *IEEE Access*, vol. 10, pp. 2646–2655, 2022.
- [15] D. F. Sievenpiper, J. H. Schaffner, H. J. Song, R. Y. Loo, and G. Tangonan, "Two-dimensional beam steering using an electrically tunable impedance surface," *IEEE Transactions on antennas and propagation*, vol. 51, no. 10, pp. 2713–2722, 2003.

- [16] X. Liu, L. Schmitt, B. Sievert, J. Lipka, C. Geng, K. Kolpatzeck, D. Erni, A. Rennings, J. C. Balzer, M. Hoffmann *et al.*, "Terahertz beam steering using a mems-based reflectarray configured by a genetic algorithm," *IEEE Access*, vol. 10, pp. 84458–84472, 2022.
- [17] D.-K. Yang and S.-T. Wu, "Fundamentals of Liquid Crystal Devices." Wiley, 2006, ch. 8. [Online]. Available: <https://www.wiley.com/en-us/Fundamentals-of-Liquid-Crystal-Devices-p-9780470032022>
- [18] R. Neuder, M. Späth, M. Schübler, and A. Jiménez-Sáez, "Architecture for sub-100 ms liquid crystal reconfigurable intelligent surface based on defected delay lines," *Communications Engineering*, vol. 3, no. 1, p. 70, 2024.
- [19] A. Jiménez-Sáez, A. Asadi, R. Neuder, M. Delbari, and V. Jamali, "Reconfigurable intelligent surfaces with liquid crystal technology: A hardware design and communication perspective," *arXiv preprint arXiv:2308.03065*, 2023.
- [20] W. Tang, M. Z. Chen, X. Chen, J. Y. Dai, Y. Han, M. Di Renzo, Y. Zeng, S. Jin, Q. Cheng, and T. J. Cui, "Wireless communications with reconfigurable intelligent surface: Path loss modeling and experimental measurement," *IEEE Transactions on Wireless Communications*, vol. 20, no. 1, pp. 421–439, 2021.
- [21] W. R. Ghanem, V. Jamali, Y. Sun, and R. Schober, "Resource allocation for multi-user downlink URLLC-OFDMA systems," in *IEEE International Conference on Communications Workshops (ICC Workshops)*, 2019, pp. 1–6.
- [22] B. Rana, S.-S. Cho, and I.-P. Hong, "Review paper on hardware of reconfigurable intelligent surfaces," *IEEE Access*, 2023.
- [23] M. Ouyang, F. Gao, Y. Wang, S. Zhang, P. Li, and J. Ren, "Computer vision-aided reconfigurable intelligent surface-based beam tracking: prototyping and experimental results," *IEEE Transactions on Wireless Communications*, 2023.
- [24] G. C. Trichopoulos, P. Theofanopoulos, B. Kashyap, A. Shekhawat, A. Modi, T. Osman, S. Kumar, A. Sengar, A. Chang, and A. Alkhateeb, "Design and evaluation of reconfigurable intelligent surfaces in real-world environment," *IEEE Open Journal of the Communications Society*, vol. 3, pp. 462–474, 2022.
- [25] J. Jeong, J. H. Oh, S. Y. Lee, Y. Park, and S.-H. Wi, "An improved path-loss model for reconfigurable-intelligent-surface-aided wireless communications and experimental validation," *IEEE Access*, vol. 10, pp. 98 065–98 078, 2022.
- [26] L. G. da Silva, P. Xiao, and A. Cerqueira, "A 2-bit tunable unit cell for 6G reconfigurable intelligent surface application," in *2022 16th European Conference on Antennas and Propagation (EuCAP)*. IEEE, 2022, pp. 1–5.
- [27] S. He, H. Yang, Y. Jiang, W. Deng, and W. Zhu, "Recent advances in MEMS metasurfaces and their applications on tunable lens," *Micromachines*, vol. 10, no. 8, p. 505, 2019.
- [28] Q. Ma, Q. Xiao, Q. R. Hong, X. Gao, V. Galdi, and T. J. Cui, "Digital coding metasurfaces: From theory to applications," *IEEE Antennas and Propagation Magazine*, vol. 64, no. 4, pp. 96–109, 2022.
- [29] J. Wu, Z. Shen, S. Ge, B. Chen, Z. Shen, T. Wang, C. Zhang, W. Hu, K. Fan, W. Padilla *et al.*, "Liquid crystal programmable metasurface for terahertz beam steering," *Applied physics letters*, vol. 116, no. 13, p. 131104, 2020.
- [30] X. Fu, L. Shi, J. Yang, Y. Fu, C. Liu, J. W. Wu, F. Yang, L. Bao, and T. J. Cui, "Flexible terahertz beam manipulations based on liquid-crystal-integrated programmable metasurfaces," *ACS Applied Materials & Interfaces*, 2022.
- [31] R. Neuder, D. Wang, R. Jakoby, and A. Jiménez-Sáez, "Compact liquid crystal-based defective ground structure phase shifter for reconfigurable intelligent surfaces," in *European Conf. Antennas and Propagation (EuCAP)*, Mar. 2023, pp. 1–5.
- [32] T. Ji, M. Hua, C. Li, Y. Huang, and L. Yang, "Robust max-min fairness transmission design for IRS-aided wireless network considering user location uncertainty," *IEEE Transactions on Communications*, vol. 71, no. 8, pp. 4678–4693, 2023.
- [33] H. Xie, J. Xu, and Y.-F. Liu, "Max-min fairness in IRS-aided multi-cell MISO systems with joint transmit and reflective beamforming," *IEEE Transactions on Wireless Communications*, vol. 20, no. 2, pp. 1379–1393, 2021.
- [34] H. Yu, H. D. Tuan, A. A. Nasir, E. Dutkiewicz, and L. Hanzo, "Rate-fairness-aware low resolution RIS-aided multi-user OFDM beamforming," *IEEE Transactions on Vehicular Technology*, vol. 73, no. 2, pp. 2401–2415, 2024.
- [35] Q. Tao, S. Zhang, C. Zhong, W. Xu, H. Lin, and Z. Zhang, "Weighted sum-rate of intelligent reflecting surface aided multiuser downlink transmission with statistical CSI," *IEEE Transactions on Wireless Communications*, vol. 21, no. 7, pp. 4925–4937, 2022.
- [36] Z. Li, M. Hua, Q. Wang, and Q. Song, "Weighted sum-rate maximization for multi-IRS aided cooperative transmission," *IEEE Wireless Communications Letters*, vol. 9, no. 10, pp. 1620–1624, 2020.
- [37] Y. Song, S. Xu, G. Sun, and B. Ai, "Weighted sum-rate maximization in multi-IRS-aided multi-cell mmWave communication systems for suppressing ICI," *IEEE Transactions on Vehicular Technology*, vol. 72, no. 8, pp. 10 234–10 250, 2023.
- [38] C. Huang, A. Zappone, G. C. Alexandropoulos, M. Debbah, and C. Yuen, "Reconfigurable intelligent surfaces for energy efficiency in wireless communication," *IEEE Transactions on Wireless Communications*, vol. 18, no. 8, pp. 4157–4170, 2019.
- [39] W. Zhong, Z. Yu, Y. Wu, F. Zhou, Q. Wu, and N. Al-Dhahir, "Resource allocation for an IRS-assisted dual-functional radar and communication system: Energy efficiency maximization," *IEEE Transactions on Green Communications and Networking*, vol. 7, no. 1, pp. 469–482, 2023.
- [40] Q. N. Le, V.-D. Nguyen, O. A. Dobre, and R. Zhao, "Energy efficiency maximization in RIS-aided cell-free network with limited backhaul," *IEEE Communications Letters*, vol. 25, no. 6, pp. 1974–1978, 2021.
- [41] X. Mu, Y. Liu, L. Guo, J. Lin, and R. Schober, "Simultaneously transmitting and reflecting (STAR) RIS aided wireless communications," *IEEE Transactions on Wireless Communications*, vol. 21, no. 5, pp. 3083–3098, 2022.
- [42] Y. Zhou, Y. Liu, Q. Wu, Q. Shi, J. Zhao, and Y. Zhao, "Queueing aware power minimization for wireless communication aided by double-faced active RIS," *IEEE Transactions on Communications*, vol. 71, no. 10, pp. 5799–5813, 2023.
- [43] Q. Wang, X. Pang, C. Wu, L. Xu, N. Zhao, and F. R. Yu, "Transmit power minimization for STAR-RIS aided FD-NOMA networks," *IEEE Transactions on Vehicular Technology*, vol. 73, no. 3, pp. 4389–4394, 2024.